magnetochemistry

MDPI

Article

Calixarene-like Lanthanide Single-Ion Magnets Based on Nd^{III}, Gd^{III}, Tb^{III} and Dy^{III} Oxamato Complexes †

Tamyris T. da Cunha [1,2], João Honorato de Araujo-Neto [3], Meiry E. Alvarenga [4], Felipe Terra Martins [4], Emerson F. Pedroso [5], Davor L. Mariano [6], Wallace C. Nunes [7], Nicolás Moliner [8], Francesc Lloret [8], Miguel Julve [8,‡] and Cynthia L. M. Pereira [1,*]

1 Departamento de Química, Instituto de Ciências Exatas, Universidade Federal de Minas Gerais, Av. Antônio Carlos 6627, Pampulha, Belo Horizonte 31270-901, MG, Brazil
2 Campus Itabirito, Instituto Federal de Educação, Ciência e Tecnologia de Minas Gerais, R. José Benedito, 139, Santa Efigênia, Itabirito 35450-000, MG, Brazil
3 Instituto de Química, Universidade de São Paulo, Av. Prof. Lineu Prestes, 748-Butantã, São Paulo 05508-900, SP, Brazil
4 Instituto de Química, Universidade Federal de Goiás, Campus Samambaia, Setor Itatiaia, Caixa Postal 131, Goiânia 74001-970, GO, Brazil
5 Laboratório de Tecnologias Integradas (Intechlab), Centro Federal de Educação Tecnológica de Minas Gerais, Av. Amazonas 5523, Belo Horizonte 30421-169, MG, Brazil
6 Instituto de Física, Universidade Federal do Rio de Janeiro (IF-UFRJ), Av. Athos da Silveira Ramos, 149, Cidade Universitária, Rio de Janeiro 24210-340, RJ, Brazil
7 Instituto de Física, Universidade Federal Fluminense, Av. Gal. Milton Tavares de Souza, s/nº, Campus da Praia Vermelha, Niterói 24210-346, RJ, Brazil
8 Departament de Química Inorgànica, Instituto de Ciencia Molecular (ICMol), Universitat de València, C/Catedrático José Beltrán 2, 46980 Paterna, València, Spain
* Correspondence: cynthialopes@ufmg.br

† We dedicate this manuscript to Prof. Francesc Lloret and Prof. Miguel Julve, brilliant scientists, to honor their careers on the occasion of their retirement.

‡ Prof. Miguel Julve passed away while preparing this contribution. We do not have words to express our feelings. Still, we are very grateful for the luck of knowing Prof. Miguel Julve, a beautiful person, beloved friend, and tireless scientific collaborator. Thank you, Miguel.

Abstract: In this work, we describe the synthesis, crystal structures and magnetic properties of four air-stable mononuclear lanthanide(III) complexes with the *N*-(2,4,6-trimethylphenyl)oxamate (Htmpa) of formula: *n*-Bu_4N[Nd(Htmpa)$_4$(H_2O)]·4H_2O (**1**), *n*-Bu_4N[Gd(Htmpa)$_4$(H_2O)]·3DMSO·2H_2O (**2**), *n*-Bu_4N[Tb(Htmpa)$_4$(H_2O)]·3DMSO·1H_2O (**3**) and *n*-Bu_4N[Dy(Htmpa)$_4$(H_2O)]·3DMSO·2H_2O (**4**) (*n*-Bu_4N^+ = *n*-tetrabutylammonium; DMSO = dimethylsulfoxide). Their crystal structures reveal the occurrence of calixarene-type monoanionic species containing all-*cis*-disposed Htmpa ligands and one water molecule coordinated with the respective Ln^{III} ion (Ln = Nd, Gd, Tb and Dy), featuring a nine-coordinated environment with muffin (MFF-9) (**1**) or spherical-capped square antiprism (CSAPR-9) (**2**–**4**) geometry. The major difference between their crystal structures is related to the nature of crystallization solvent molecules, either water (**1**) or both DMSO and water (**2**–**4**). The intermolecular hydrogen bonds among the self-complementary Htmpa ligands in all four compounds mediated a 2 D supramolecular network in the solid state. Direct-current (dc) magnetic properties for **1**–**4** show typical behavior for the ground state terms of the Ln^{III} ions [$^4I_{9/2}$ (Nd); $^8S_{7/2}$(Gd), $^7F_6$ (Tb), $^6H^{15/2}$ (Dy)]. Alternating-current (ac) magnetic measurements reveal the presence of slow magnetic relaxation without the presence of a dc field only for **4**. In contrast, field-induced slow magnetic relaxation behavior was found in complexes **1**, **2** and **3**.

Keywords: oxamate; lanthanide; single-ion magnet; supramolecular chemistry; neodymium(III); gadolinium(III); terbium(III); dysprosium(III)

check for updates

Citation: da Cunha, T.T.; Honorato de Araujo-Neto, J.; Alvarenga, M.E.; Martins, F.T.; Pedroso, E.F.; Mariano, D.L.; Nunes, W.C.; Moliner, N.; Lloret, F.; Julve, M.; et al. Calixarene-like Lanthanide Single-Ion Magnets Based on Nd^{III}, Gd^{III}, Tb^{III} and Dy^{III} Oxamato Complexes. *Magnetochemistry* **2024**, *10*, 103. https://doi.org/10.3390/magnetochemistry10120103

Academic Editor: Ming-Liang Tong

Received: 11 November 2024
Revised: 2 December 2024
Accepted: 3 December 2024
Published: 12 December 2024

1. Introduction

The search for new magnetic materials that exhibit slow magnetic relaxation (SMR) phenomena has received significant attention from research groups worldwide. These materials hold the potential for advancing next-generation technologies, including spin qubits and spin qudits for quantum computing, quantum information processing (QIP), spintronics and more [1].

Two synthetic strategies have been employed to obtain these materials: the "top-down" and "bottom-up" approaches. In the "top-down" approach, high-density data storage and material candidates for quantum technologies are produced by reducing the size of nanoparticles through physical methods. However, this process often results in inhomogeneous particle sizes, which is undesirable due to the lack of control over the final properties. The alternative "bottom-up" approach offers a promising route for synthesizing homogeneous molecules under mild, reproducible conditions. This method relies on self-organizing molecules exhibiting the desired properties [1]. This molecular approach employs organic linkers, enabling the incorporation of diverse paramagnetic ions to give slow-magnetic relaxing molecules, molecular assemblies or supramolecular coordination polymers [2,3].

In 2003, the discovery of terbium(III) and dysprosium(III) double-decker phthalocyanine (Pc) complexes, $(Bu_4N)[LnPc_2]$ (Ln = Tb^{3+} or Dy^{3+}), identified as single-ion magnets (SIMs), marked a significant shift in focus from polynuclear d-block complexes to mononuclear f-block systems as promising candidates for technological applications [4]. Ln SIMs, as well as Ln SMMs (SMM being single-molecule magnet), exhibited SMR and stepwise open-loop magnetic hysteresis of pure molecular origin due to the presence of a single highly anisotropic lanthanide(III) ion due to the combined effect of first-order spin-orbit coupling (SOC) and ligand-field (LF) effects that cause the splitting of the $2J + 1$ components of the ground state characterized by a total angular momentum $J = |S - L|$ or $J = S + L$ for early (Ln = Ce − Eu) or late Ln^{III} ions (Ln = Tb − Yb). In the absence of additional interactions, Kramers Ln^{III} ions (Ln = Ce^{3+}, Nd^{3+}, Sm^{3+}, Gd^{3+}, Dy^{3+}, Er^{3+}, Yb^{3+}, Lu^{3+}) are, in principle, more suitable for the development of SIMs as single-ion memory devices compared with non-Kramers ions (Ln = Pr^{3+}, Pm^{3+}, Eu^{3+}, Tb^{3+}, Ho^{3+}, Tm^{3+}). However, dipolar or hyperfine interactions can induce transverse fields that break the degeneracy of Kramers doublets ($\pm m_J$), facilitating undesired fast relaxation processes. This phenomenon is associated with quantum tunneling of magnetization (QTM) phenomena. Notably, the suppression of QTM can be achieved by diluting paramagnetic complexes within an isostructural diamagnetic matrix, thereby reducing dipolar interactions or by applying an external static magnetic field [1,5].

The magnetic properties of Ln SIMs can be modulated through ligand design. Due to the large radii of Ln^{III} ions and their electrostatic bonding, they usually form high coordination number (CN) complexes, lacking geometrical control. Several results indicate that U_{eff} increases by reducing the CN of lanthanide(III) complexes, indicating that a high axial crystal field could lead to SMR via the second and third excited states [6]. Despite Dy^{III} being a very promising ion to investigate its magnetic properties, the research diversity involving other Ln^{III} ions is crucial for scientific advancement and the development of materials for various technological applications, such as molecular magnetic refrigeration, magnetic sensors, data storage materials or light emission conversion diodes [7–10].

Our work involving molecular self-assembly of aromatic polyoxalamide ligands and lanthanide(III) ions as Ln SIMs started some years ago through the study of mononuclear dysprosium(III) complex $Me_4N[Dy(Hdmpa)_4]\cdot 2CH_3CN$ (Hdmpa = *N*-2,6-(dimethylphenyl) oxamato; Me_4N^+ is the tetramethylammonium) [11]. This complex is eight-coordinate through four oxamate ligands, arising from a hydrogen-bonded supramolecular 2D network that exhibited field-induced SIM behavior below 9.0 K with U_{eff} of ~69.1 cm^{-1}. Using the *N*-4-(hydroxyphenyl)oxamate (4-HOpa) ligand, a series of isostructural nonacoordinate complexes of formula $Na[Ln(4\text{-}HOpa)_4(H_2O)]\cdot 2H_2O$ [Ln = Dy^{3+}, Gd^{3+}, Ho^{3+} and Eu^{3+}] with a hydrogen-bonded 2D supramolecular was described [12]. The dysprosium(III) and

gadolinium(III) complexes exhibited SMR phenomena below 10 K. In principle, SMR behavior was not expected for the magnetically isotropic Gd^{III} ion because it does not present SOC. Its ground state is $^8S_{7/2}$ with no angular momentum [13], so the energy barrier for spin reversal is very small because of the negligible value of the zero-field splitting component (D~0.1 cm^{-1}). Hence, to observe SMR in Gd^{3+} ions, the metal environments should be distorted, leading to a specific anisotropy by mixing the low-lying states. This behavior can also occur with 3d-block ions like high-spin Mn^{2+} ions in octahedral environments ($^6A_{1g}$), which shows a negligible D value (D~0.1 cm^{-1}) [14]. Therefore, field-induced SMR behavior could appear in Gd^{3+} or Mn^{2+} complexes and is unrelated to a significant energy barrier. More recently, we demonstrated that by increasing the rigidity of the crystal structure, as in the 1D coordination polymer $\{Gd(Hphpa)_3(DMSO)_2\}_n \cdot nH_2O$ [Hphpa = *N*-(phenyl)oxamate (DMSO = dimethylsulfoxide)], field-induced SMR appeared below 33 K, the highest temperature range found for gadolinium(III) complex up to date [15].

The first examples of Ln SIMs with calixarene-like oxamate motifs were reported a few years ago. These compounds were synthesized using the *N*-(4-Xphenyl)oxamate ligands (H-4-Xphpa with X = Cl or F), affording isostructural compounds of formula n-$Bu_4N[Ln(4\text{-}Xphpa)_4(H_2O)] \cdot nH_2O$ (n-Bu_4N^+ = n-tetrabutylammonium with Ln = Eu, Gd, Dy, Tb, Nd, Ho, Y and La) [16,17]. In this series, the crystal structures remember a calixarene structure, but there is no connection between the phenyl rings, as seen in a classical calixarene. The connection is achieved by the Ln^{III} ion through the coordination to the oxygen atoms from the all-*cis*-disposed ligands so that each aromatic ring is almost facing one another, remembering a calyx, with a *trans* apical solvent molecule completing the nine-coordinate sphere of the Ln^{III} ion. In such complexes, only Gd^{3+}, Dy^{3+}, Tb^{3+} and Ho^{3+} compounds present field-induced SMR behavior, in which an energy barrier of 66 cm^{-1} was observed for the Dy^{3+} complex below 7.0 K.

Recently, the gadolinium complex $Na[Gd(4\text{-}HOpa)_4(H_2O)] \cdot 2H_2O$ was successfully tested as a spin qubit, so that is a suitable candidate for quantum technologies below 10 K [18]. Its diamagnetically diluted complex (1Gd0.12%) with yttrium shows relatively high spin-lattice and spin-relaxation times (T_1 = 1.66 ms at 4 K and T_m = 4.25 µs at 8 K).

In this contribution, we report the synthesis, crystal structures and magnetic properties of the novel series of mononuclear lanthanide(III) complexes with the *N*-(2,4,6-trimethylphenyl)oxamate ligand (Htmpa) of general formula n-$Bu_4N[Ln(Htmpa)_4(H_2O)] \cdot xDMSO \cdot yH_2O$ [Ln = Nd^{3+} (**1**), Gd^{3+} (**2**), Tb^{3+} (**3**) and Dy^{3+} (**4**), with x = 0 and y = 4 (**1**), x = 2 and y = 2 (**2** and **4**), and x = 2 and y = 1 (**3**)] (Scheme 1). Complexes **1**–**3** behave as field-induced SIMs, while **4** exhibits SIM behavior without applying an external magnetic field.

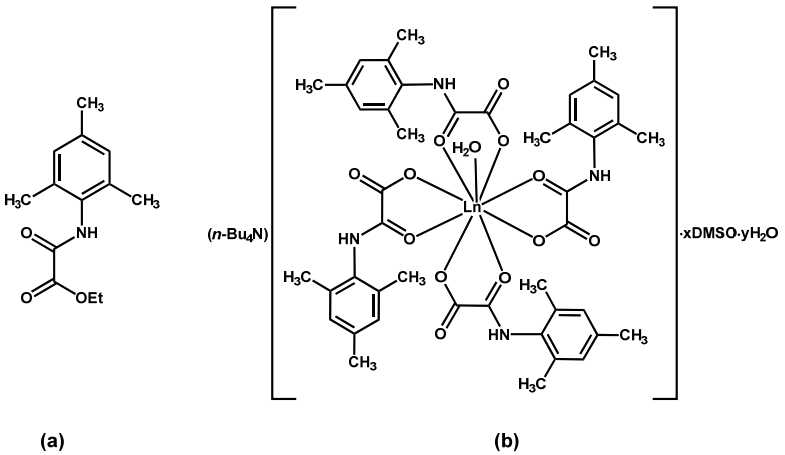

Scheme 1. (**a**) Chemical structure of the proligand *N*-(2,4,6-trimethylphenyl)oxamic acid ethyl ester (EtHtmpa) and (**b**) their mononuclear lanthanide(III) oxamate complexes.

2. Experimental

2.1. Materials and Methods

All chemicals and solvents used in this work were of analytical grade and used as received. The proligand EtHtmpa was obtained as previously reported [19,20]. Elemental analyses (CHN) were carried out with a Perkin-Elmer 2400 analyzer. IR spectra were recorded from KBr pellets on a PerkinElmer 882 spectrophotometer in the 4000 and 400 cm^{-1} range. The thermal analysis (TG/DTA, thermogravimetric/differential thermal analysis) was conducted with a DTG-60H Shimadzu instrument using ~3.0 mg of each complex placed individually in an alumina crucible. The solid samples were heated at 10 °C min^{-1} from room temperature to 700 °C under a synthetic air atmosphere (flow rate of 100 mL min^{-1}). X-ray powder diffraction patterns (PXRD) were taken on the Shimadzu XRD-7000 X-ray equipment, using CuK_{α} radiation (λ = 1.54056 Å), in the 4–40° range, with the goniometer speed equal to 0.5 °min^{-1} and 1 s of sampling time. The simulated PXRD patterns were generated with Mercury software (version 2022.3.0), using the crystal data from the single-crystal X-ray diffraction cif files [21].

2.2. Magnetic Measurements

Variable-temperature (2–300 K) direct current (dc) magnetic susceptibility under applied fields of 0.20 kOe or 5.0 kOe were carried out using a Quantum Design SQUID magnetometer model MPMS-XL-5. Variable-field magnetization measurements were carried out using a Quantum Design SQUID magnetometer model MPMS-XL-5 at 2, 3, 4, 5, 7 and 10 K. Variable-temperature alternate current (ac) magnetic susceptibility measurements were carried out using a Model Quantum Design PPMS-9 operating with a small amplitude ac field (5 Oe) and scanning within the frequency range of 0.1–10 kHz at different applied dc magnetic fields for complexes **1**–**4**. The dc and ac measurements were carried out in polycrystalline samples of complexes **1**–**4**, previously placed in a gelatin capsule and with eicosane to prevent crystal movement. Corrections of diamagnetism of the samples and for the sample holder were also applied.

2.3. Crystal Data Collection and Refining

X-ray diffraction data collections on single crystals of compounds **1**–**4** were performed using a Rigaku Synergy diffractometer with a Mo-Kα (0.71073 Å) source at 293 K. The structures were solved using the SHELXS program (Version 2014/6) in Olex2 suit [22,23]. Data integration and scaling of the reflections for all compounds were performed with the CRYSALISPRO 43.90 suite [24]. Final unit cell parameters were based on the fitting of all reflection positions. Analytical absorption corrections and space group identification were performed using the CRYSALISPRO 43.90 suite [24]. Their structures were solved by direct methods using the SUPERFLIP 1.0 program [25]. The solvent mask tool from the Olex2 program was utilized to mask disordered solvents during the final refinement [23]. The corresponding electron counts removed were equivalent to 2.4 water molecules (24 electrons) for complex **1**, 1.1 DMSO molecules (46 electrons) for complex **2**, 0.6 water molecules (6 electrons) and 0.9 DMSO molecules (38 electrons) for complex **3** and 1.1 DMSO molecules (46 electrons) for complex **4**. For each compound, the positions of all atoms could be unambiguously assigned on consecutive difference Fourier maps. Refinements were performed using SHELXL based on F2 through the full-matrix least-square routine [26]. All non-hydrogen atoms were refined with anisotropic atomic displacement parameters. All hydrogen atoms were located in different maps and included as fixed contributions according to the riding model [27]. For the aromatic carbon atoms and amine groups C–H = 0.97 Å, N–H = 0.86 Å and $U_{iso}(H) = 1.2\ U_{eq}(C/N)$, for aliphatic carbon atoms C–H and N–H = 0.96 Å and $U_{iso}(H) = 1.5$ Ueq(C/N) and finally for water molecules O–H = 1.00 Å and $U_{iso}(H) = 1.5\ U_{eq}(O)$. Molecular graphics were generated with MERCURY software (version 2022.3.0) [21]. Crystal data, experimental details and refinement results are summarized in Table 1.

Table 1. X-ray diffraction data collection and refinement parameters for complexes **1**–**4**.

Compound	1	2	3	4
Formula	$C_{60}H_{90.8}N_5O_{15.4}Nd$	$C_{66.2}H_{106.6}N_5O_{17}S_{3.1}Gd$	$C_{65.8}H_{104.6}N_5O_{16.5}S_{2.9}Tb$	$C_{66.2}H_{106.6}N_5O_{17.1}S_{3.1}Dy$
MW/g mol^{-1}	1272.85	1502.79	1481.63	1508.04
T/K	293	293	293	293
λ/Å	0.71073	0.71073	0.71073	0.71073
Crystal system	Monoclinic	Monoclinic	Monoclinic	Monoclinic
Space group	$P2/n$	$P2_1/n$	$P2_1/n$	$P2_1/n$
a/Å	21.5741(6)	15.4140(3)	15.4180(5)	15.4368(4)
b/Å	11.9763(3)	30.8190(8)	30.8696(11)	30.8542(12)
c/Å	25.0931(7)	16.1547(4)	16.0716(5)	16.1669(4)
β/°	90.861(3)	90.248(2)	90.250(3)	90.165(2)
V/Å^3	6482.8(3)	7674.1(3)	7649.2(4)	7700.1(4)
Z	4	4	4	4
ρ/Mg m^{-3}	1.260	1.226	1.216	1.301
μ/mm^{-1}	0.862	0.979	1.038	1.118
F(000)	2580.0	2972.0	2936.0	3165.0
Reflections collected	12,320	14,582	14,533	88,831
R [a], wR [b] [I > 2σ(I)]	0.0522;0.1223	0.0572, 0.1518	0.0626, 0.1616	0.0529, 0.1119
R [a], wR [b] (all data)	0.0570	0.0839	0.0874	0.0786
S [c]	1.053	1.164	1.088	1.124
ρ_{max} and ρ_{min}/e Å$^-$	0.9759/–1.3070	3.598/–1.417	3.153/–1.619	2.87/–1.08
CCDC	2,380,352	2,380,353	2,380,351	2,380,354

[a] $R = \Sigma \; | \; |F_o| - |F_c| \; | \; / \Sigma \; |F_o|$. [b] $wR = [\Sigma \, w(|F_o|^2 - |F_c|^2)^2 / \Sigma \, w|F_o|^2]^{1/2}$. [c] $S = [\Sigma \, w(|F_o|^2 - |F_c|^2)^2 / (n_o - np)]^{1/2}$, where $w \propto 1/\sigma$, n_o = observed and n_p = fitted parameters.

*2.4. General Procedure for Synthesis of Compounds n-Bu$_4$N[Ln(Htmpa)$_4$(H$_2$O)]·xDMSO·yH$_2$O [Ln = Nd^{3+} (**1**), Gd^{3+} (**2**), Tb^{3+} (**3**) and Dy^{3+} (**4**)]*

A mixture was prepared by combining deionized water (30 mL), the proligand EtHtmpa (480 mg, 2.04 mmol) and tetrabutylammonium hydroxide solution 40% w/v in water (1.33 mL, 2.04 mmol). This resultant mixture was maintained at 60 °C for 30 min under continuous stirring. After the hydrolysis, the mixture was cooled to room temperature, and dimethylsulfoxide (42 mL) was added. Subsequently, a solution containing the correspondent metal salt (0.51 mmol) previously dissolved in deionized water (6.0 mL) was added dropwise with constant agitation. The resulting mixture was heated to 60 °C for 15 min and then filtered, leaving the filtrate to rest at room temperature. After 5 days, suitable crystals for X-ray diffraction experiments were obtained. These crystals were filtered and air-dried at room temperature for 24 h. The correspondent salts employed in the synthesis were Ln(CH$_3$COO)$_3$·nH$_2$O [Ln = Nd^{3+} (n = 1); Gd^{3+} (n = 4), Dy^{3+} (n = 3)] or TbCl$_3$·6H$_2$O.

n-Bu$_4$N[Nd(Htmpa)$_4$(H$_2$O)]·4H$_2$O (**1**): yield 54% (362 mg; 0.28 mmol). Elemental analysis (calcd.) for $C_{60}H_{94}N_5O_{17}Nd$ (1301.67 g mol^{-1}): C 54.89 (55.36), H 6.95 (7.28), N 4.99 (5.38)%. IR (KBr, cm^{-1}): 3424 (ν_{O-H}), 3342, 3250 (ν_{N-H}), 2962, 2924 and 2874 (ν_{C-H}), 1654 ($\nu_{C=O}$), 1528, 1484 ($\nu_{C=C}$), 1374 (δ_{N-H}), 1232 (ν_{C-O}), 850, 766 (γ_{C-H}) cm^{-1}.

n-Bu$_4$N[Gd(Htmpa)$_4$(H$_2$O)]·3DMSO·2H$_2$O (**2**): yield 31% (222 mg; 0.15 mmol). Elemental analysis (calcd.) for $C_{66}H_{108}N_5O_{18}S_3Gd$ (1513.04 g mol^{-1}): C 52.32 (52.39), H 7.09 (7.20), N 4.82 (4.63)%. IR (KBr, cm^{-1}): 3422 (ν_{O-H}), 3328, 3224 (ν_{N-H}), 2966, 2918, 2876 (ν_{C-H}), 1644 ($\nu_{C=O}$), 1534, 1486 ($\nu_{C=C}$), 1374 (δ_{N-H}), 1240 (ν_{C-O}), 1030 ($\nu_{S=O}$), 852, 766 (γ_{C-H}) cm^{-1}.

n-Bu$_4$N[Tb(Htmpa)$_4$(H$_2$O)]·3DMSO·1H$_2$O (**3**): yield 64% (490 mg; 0.33 mmol). Elemental analysis (calcd.) for $C_{66}H_{106}N_5O_{17}S_3Tb$ (1496.70 g mol^{-1}): C 52.88 (52.97), H 6.94 (7.14), N 4.78 (4.68)%. IR (KBr, cm^{-1}): 3422 (ν_{O-H}), 3328, 3224 (ν_{N-H}), 2966, 2920, 2876 (ν_{C-H}), 1644 ($\nu_{C=O}$), 1534, 1486 ($\nu_{C=C}$), 1376 (δ_{N-H}), 1240 (ν_{C-O}), 1028 ($\nu_{S=O}$), 852, 768 (γ_{C-H}) cm^{-1}.

n-Bu_4N[Dy(Htmpa)$_4$(H_2O)]·3DMSO·2H_2O (**4**): yield 67% (490 mg; 0.32 mmol). Elemental analysis (calcd.) for $C_{66}H_{108}N_5O_{17}S_3Dy$ (1518.29 g mol^{-1}): C 52.93 (52.21), H 6.78 (7.17), N 4.78 (4.61)%. IR (KBr, cm^{-1}): 3422 (ν_{O-H}), 3328, 3224 (ν_{N-H}), 2966, 2918, 2878 (ν_{C-H}), 1644 ($\nu_{C=O}$), 1534, 1486 ($\nu_{C=C}$), 1376 (δ_{N-H}), 1240 ($\nu_{S=O}$), 1026 ($\nu_{S=O}$), 852, 768 (γ_{C-H}) cm^{-1}.

3. Results and Discussion

Complexes **1–4** were synthesized through the in situ hydrolysis of the ethyl ester with tetrabutylammonium hydroxide, as described for several oxamate complexes containing transition metal ions of the first series [28,29], followed by a stoichiometric reaction with the correspondent lanthanide(III) acetate salt in DMSO/water solution (Scheme 2). In this contribution, we demonstrate again that it is possible to obtain the lanthanide(III) oxamate compounds through one-pot synthesis without isolation of the *n*-Bu_4N(EtHmpa) salt [20]. Single crystals of the appropriate quality to solve the crystal structure using an X-ray diffraction experiment were obtained.

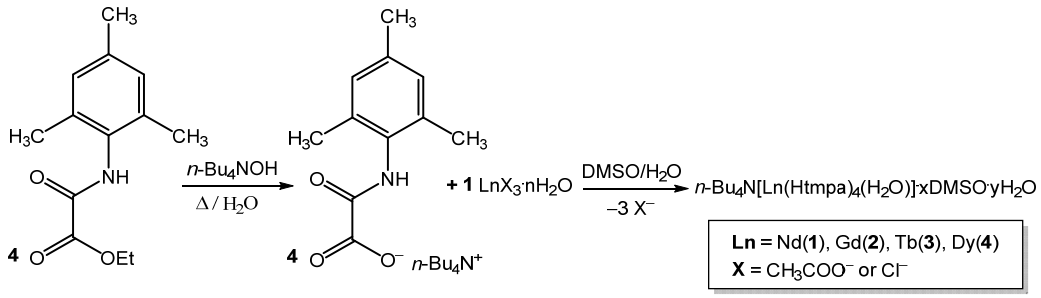

Scheme 2. Synthetic procedure for complexes **1–4**.

Elemental analysis, IR spectroscopy and thermogravimetric analysis confirm the chemical structure of all compounds. The IR spectra of complexes **1–4** (Figure S1) are very similar and exhibit the characteristic stretching vibrations corresponding to the presence of OH groups (3424–3422 cm^{-1}) and NH groups (3328 and 3224 cm^{-1}) [20]. Additionally, the downward shifting of the stretching vibrations of C=O groups (1654–1644 cm^{-1}) relative to the proligand EtHtmpa (1732 and 1680 cm^{-1}) is strong evidence of the ester hydrolysis and further coordination of these groups to metal ions.

Thermal analysis (TG/DTA) for complexes **1–4** (Figures S2–S5) agrees with the results proposed by elemental analysis and SCXRD data. For **1**, the first weight loss event (4.9%) occurs in the 38–140 °C range, corresponding to the release of approximately 3.6 water molecules (calcd.: 4.8%). Then, upon continuous heating until 250 °C, a small weight loss occurs (0.6%), which can be associated with 0.4 water molecules (calcd.: 0.4%). Complex **2** exhibits two weight losses from room temperature to 135 °C, running at two steps. The first one, in the range of 38–100 °C (6.7%), involves releasing one DMSO and one water molecule of crystallization (calc.: 6.3%). Then, upon heating, a second weight loss occurs until 149 °C (12.5%), associated with the loss of two DMSO molecules of crystallization and one water of coordination (calcd.: 12.6%). The resulting unsolvate species *n*-Bu_4N[Gd(Htmpa)$_4$] is stable until 229 °C, when further heating provides the decomposition of the complex. The TG curves of **3** and **4** have a similar profile, with two events occurring from room temperature until 142 °C for **3** and 147 °C for **4**. From room temperature until 90 °C, a loss of 6.44% (calcd.: 6.38%) and 6.36% (calcd.: 6.40%) of the initial mass occurs for **3** and **4**, respectively. It can be associated with releasing one DMSO and one water crystallization molecule. Upon continuous heating, a second event occurs at 142 °C (**3**) and 146.5 °C (**4**), releasing 10.56% (**3**) and 11.69% (**4**) of the mass, which corroborates the removal of two DMSO crystallization molecules for **3** (calcd.: 10.37%) and two DMSO and one water crystallization molecule for **4** (calcd.: 11.60%).

The X-ray diffraction patterns of **2**–**4** are similar, differing from **1** (Figures S6–S9), confirming their isostructurality. Yet, all of them agree with the simulated X-ray diffraction patterns extracted from the correspondent retrieved from the cif files, suggesting that the bulks have the same structure as the single crystals, supporting the purity of the samples.

3.1. Crystal Structures

Complex **1** crystallizes in the *P*2/*n* space group of the monoclinic system, with different unit cell dimensions for **1** compared to **2**–**4**, which in turn are then stated to be isostructural and crystallize in the $P2_1/n$ space group. In fact, **1** differs from **2**–**4** regarding the spatial organization of mononuclear units and the nature and number of crystallization solvent molecules. Hence, **1** presents four crystallization water molecules, while **2** and **4** present two water and three DMSO molecules. The thermal analysis of **3** revealed one water and three DMSO molecules of crystallization. There is some difference in water content found from crystal structure refinement and TG/elemental analysis, which can be assigned either to non-structural hydration or to smeared electron density corresponding to disordered structural water, which cannot be distinguished from residual electronic density in crystal structures bearing heavy metal atoms.

Due to the lanthanide contraction caused by the progressive electron occupation of the inner 4f orbitals, the radii of the lanthanides decrease slowly along the lanthanide series. Therefore, the ability to accommodate ligands around the Ln^{3+} cation is similar for the series, consistent with the structural variations observed among the monomers in this series. Thus, due to the similarities between all three structures of **2**–**4**, we selected the structure of **3** for a detailed discussion when compared to that of **1**.

The structures of **1** and **3** comprise four all-*cis*-disposed Htmpa ligand units, one coordinated water molecule and a nine-coordinate metal center, forming a monoanionic complex. To neutralize the charge system, there is an *n*-tetrabutylammonium cation, in addition to four crystallization water molecules (**1**) or one water molecule and three crystallization DMSO molecules (**3**) (Figure 1). Selected bond lengths and angles for **1**–**4** are listed in Tables S1–S4.

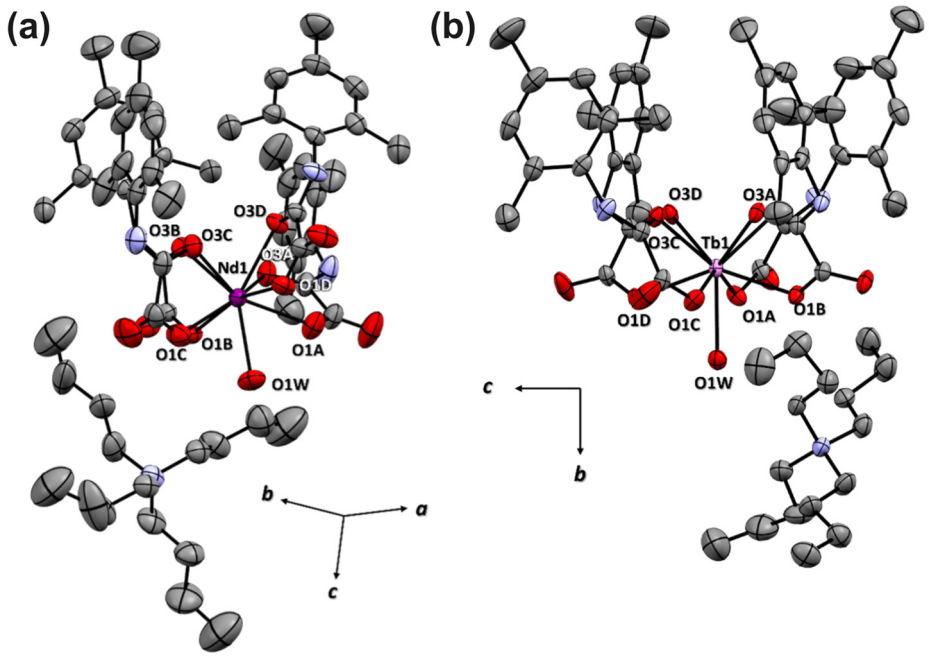

Figure 1. ORTEP view of the crystal structures of (**a**) **1** and (**b**) **3**. Crystallization water molecules and hydrogen atoms have been omitted for clarity, and ellipsoids represent 50% probability levels.

The coordination sphere of the nine-coordinate metal center in **1** and **3** consists of eight carbonyl oxygen atoms from the carboxylate amide groups of the four chelating

oxamate ligands, as well as the O1W atom from the coordinated water molecule (Figure 2). According to the SHAPE software (version 2.0) [30], the coordination geometry of **2**–**4** corresponds to the CSAPR-9 (spherical capped square antiprism, C_{4v}), while **1** corresponds to the MFF-9 (Muffin, C_s) (Table S9). The values of the SHAPE parameters [S(MFF) = 1.640 (**1**), and S(CSAPR) = 0.379(**2**)/0.322(**3**)/0.383(**4**)] indicate that distortion concerning the ideal CSAPR-9 symmetry increases in the following order: **3** < **2** < **4**.

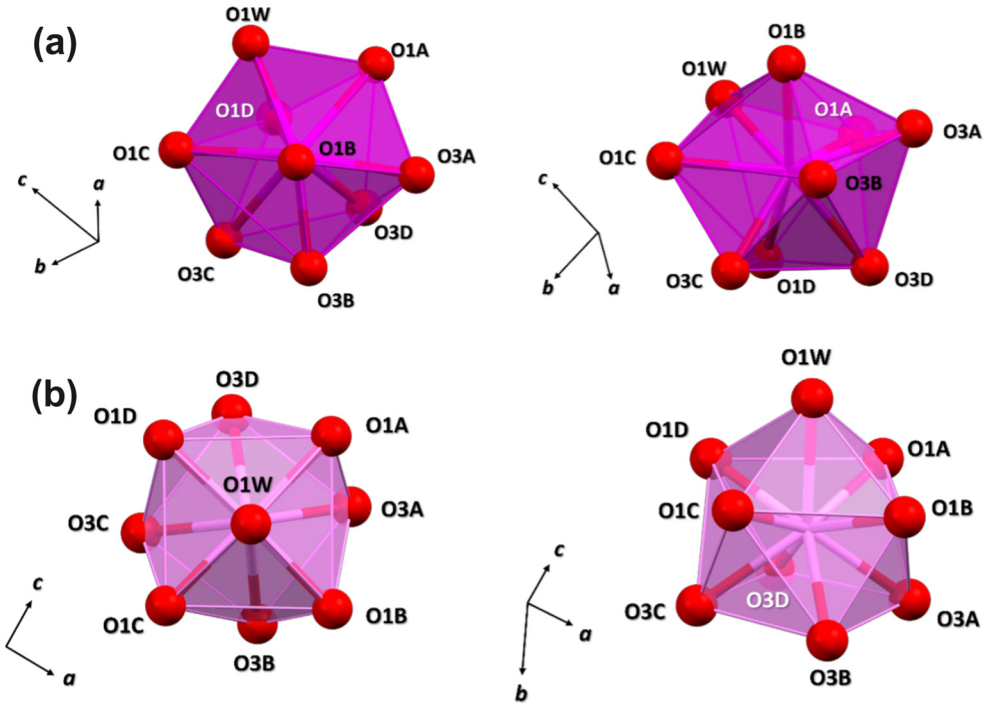

Figure 2. (**a**) Top and side views of the coordination polyhedron around the Nd1 metal center of **1** with the atom numbering scheme for the donor atoms, showing the distorted muffin geometry. The O1D/O3C/O3D atoms compose the triangular base, and the O1A/O1C/O3A/O3B/O1w atoms compose the pentagonal plane with the O1B atom in the capped position. (**b**) Top and side views of the coordination polyhedron around the Tb1 metal center of **3** with the atom numbering scheme for the donor atoms, showing the distorted capped square antiprism geometry. The O3A/O3B/O3C/O3D atoms compose the square base of the prism, and the O1A/O1B/O1C/O1D atoms compose the quadratic plane of the capped face with the O1W atom in the capped position.

The four units are pointed in the same direction in both **1** and **3**, forming a calixarene-like species around the metal center (Figure 1). In the crystal lattice of **3**, the adjacent mononuclear units interact with each other through self-complementary double hydrogen bonds between the N–H and C=O groups from each of the four Htmpa ligands leading to supramolecular layers growing within the *ac* (**3**) plane (Figure 3b). These layers are assembled glide-plane symmetry-related molecules, which are placed alternately pointing up and down into the hydrogen-bonded chains grown along the [101] and [−101] directions for the bi-dimensional layer. The shortest intermetallic distances between neighboring hydrogen-bonded units along the [101] and [−101] are 11.158 and 11.206 Å (**2**), 11.128 and 11.177 Å (**3**) and 11.179 and 11.211 Å (**4**). In **1**, the two-dimensional layer is also assembled, but it is moved onto the *ab* plane. The self-complementary double hydrogen bonds between the N–H and C=O groups also occur in this layer, but only along the [100] direction wherein inversion symmetry molecules are alternately placed as in **3**. The shortest two distinct intrachain intermetallic distances along [100] are 11.466 and 11.443 Å in **1**. However, different from **3**, there are no self-complementary double hydrogen bonds between the N–H and C=O groups in the other chain growing [010] direction responsible for mounting the dimensional layer. In this pattern, there are only N–H···O=C hydrogen

bonds between neighboring translation symmetry-related molecules, which, therefore, are not alternately placed but always pointing towards the same side. The shortest two distinct intrachain intermetallic distances along [010] are 12.665 and 11.976 Å in **1**.

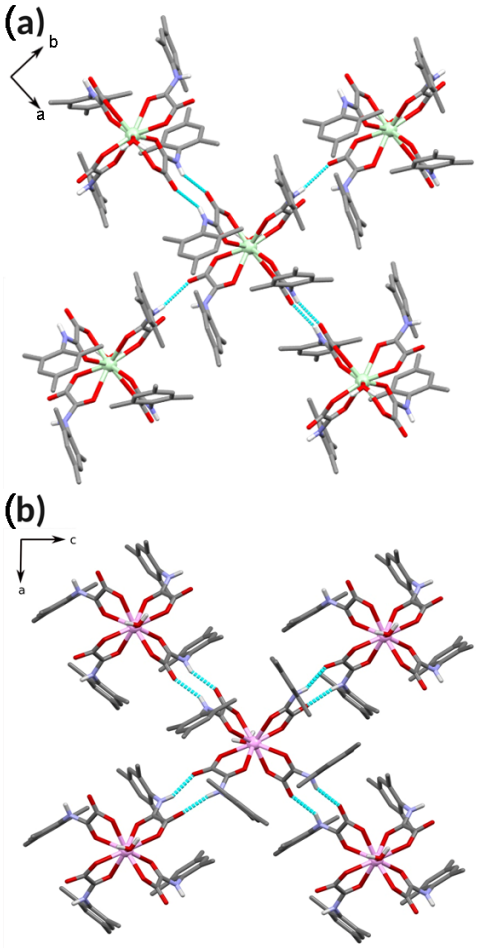

Figure 3. (**a**) View of the supramolecular layers of hydrogen-bonded mononuclear units of **1** along the crystallographic *ab* plane. (**b**) View of the supramolecular layers of hydrogen-bonded mononuclear units of **3** along the crystallographic *ac* plane, showing the presence of additional hydrogen-bonded DMSO molecules. Cyan dashed lines represent hydrogen bonds. CH hydrogen atoms, remaining solvent molecules and tetrabutylammonium cations were omitted for the sake of clarity.

These intralayer hydrogen-bonded supramolecular synthons are classified by Etter as $R_2^2(10)$ (Figure 3), except for that responsible for assembling the chain along the [010] in **1**, which is as defined as $C(8)$ [31]. The layers of **1** and **3** are packed differently, including the distinct disposition of tetrabutylammonium cations among them (Figure 4), which are involved in weaker non-classical hydrogen bonds and vdW interactions with the molecules of the complexes. In addition, there is a complex pattern of interlayer hydrogen bonding interactions between coordinated and crystallization DMSO and water molecules governing the 3D self-assembly of the system. Selected intra- and interlayer hydrogen bond lengths and angles for **1**–**4** are listed in Tables S5–S8.

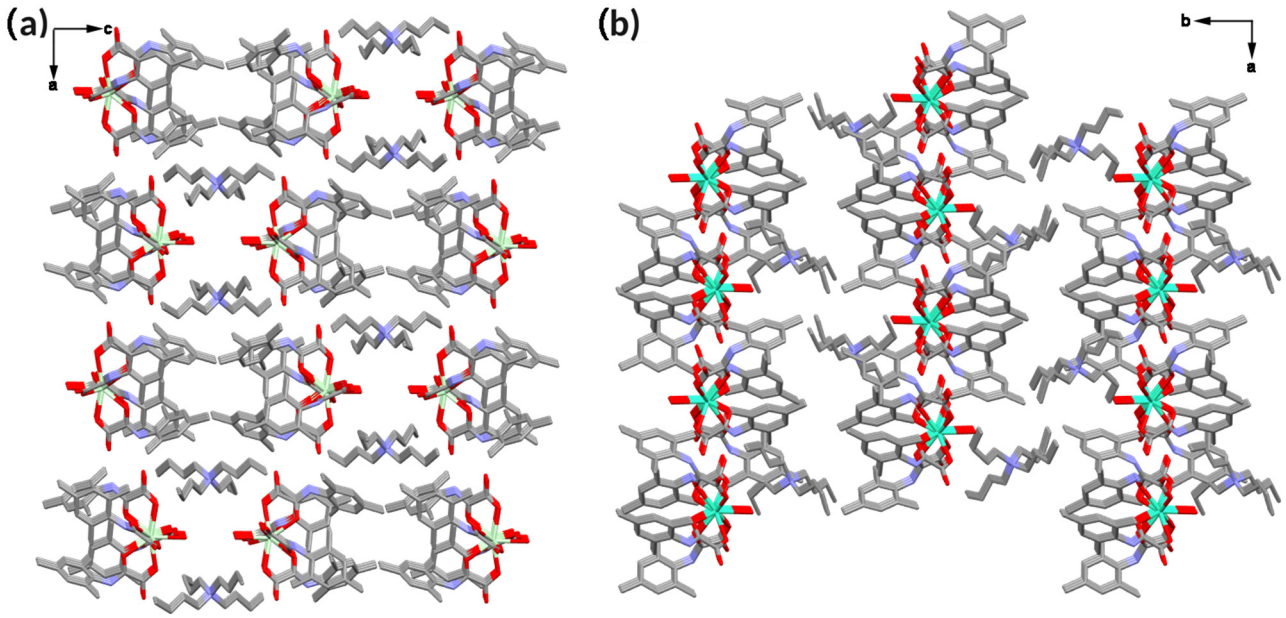

Figure 4. Views perpendicular to the layers growing onto the (**a**) *ab* plane in **1** and (**b**) *ac* plane in **3**. Three layers are depicted in each panel, while hydrogen atoms and solvent molecules were omitted for the sake of clarity. Color codes: carbon, gray; nitrogen, light blue; oxygen, red; Nd, light green; and terbium, green.

3.2. Static Magnetic Properties

Static direct current (dc) magnetic properties for **1–4** are presented in Figure 5 as the $\chi_M T$ vs. T and M vs. H curves (χ_M and M being the molar dc magnetic susceptibility and magnetization per mononuclear unit). The M vs. H/T curves are shown in Supplementary Materials (Figure S10). Table 2 summarizes all magnetic data for **1–4**.

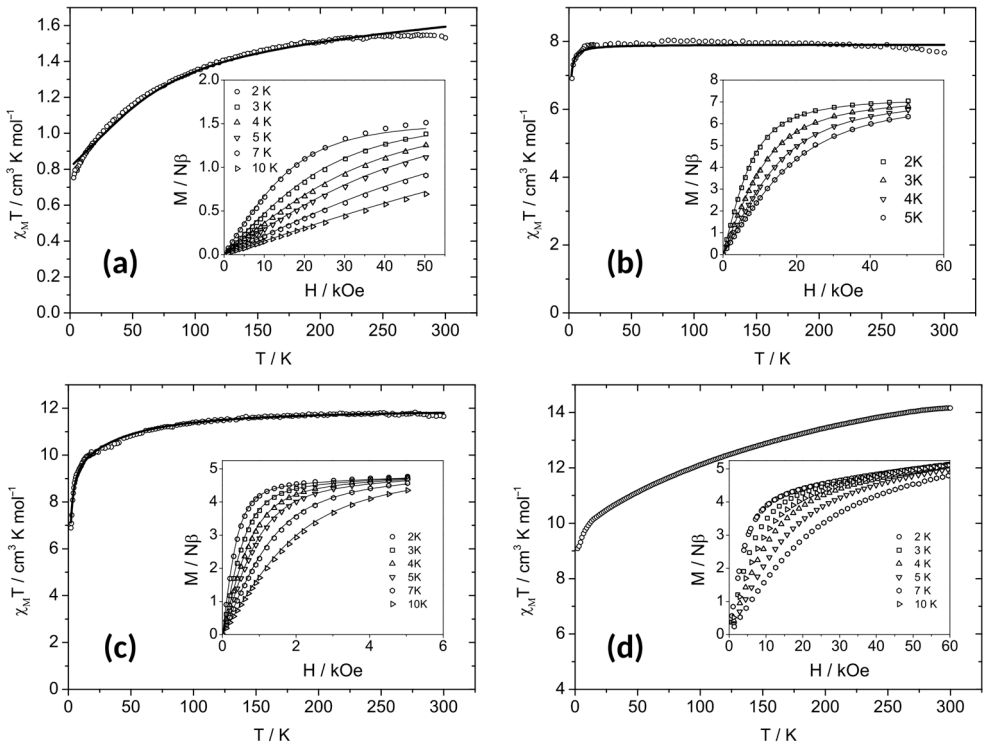

Figure 5. $\chi_M T$ vs. T curves for **1–4** (**a–d**). Inset: M vs. H curves. Solid lines represent the best-fit curves according to the text.

Table 2. Experimental and calculated magnetic dc data for compounds **1**–**4**.

Complex	Theory					$\chi_M T$ (cm^3 K mol^{-1}) Calculated	$\chi_M T$ (cm^3 K mol^{-1}) Experimental	Fitting Parameters				ΔE [1] (cm^{-1})
	g	S	L	J	Free Ion Term			λ (cm^{-1})	Δ (cm^{-1})	g	zJ (cm^{-1})	
1	8/11	3/2	6	9/2	$^4I_{9/2}$	1.64	1.53	+258.94	+55.45			1639
2	2	7/2	0	7/2	$^8S_{7/2}$	7.88	7.20			2.0	−0.01	
3	3/2	3	3	6	$^7F_6$	11.82	11.65	−387.29	−48.64		−0.02	1936
4	4/3	5/2	5	15/2	$^6H_{15/2}$	14.17	14.16					

[1] $\Delta E = -J|\lambda|$.

For the neodymium(III) complex **1**, a $\chi_M T$ value of 1.53 cm^3 K mol^{-1} (Figure 5a) is observed at room temperature, which is slightly below the expected value for a Nd^{3+} ion with a $^4I_{9/2}$ ground state, well-separated from the first $^4I_{11/2}$ excited state, in a free ion approximation (1.64 cm^3 K mol^{-1}, with $J = 9/2$ and $g_J = 8/11$). Cooling the sample, the $\chi_M T$ value decreases sharply, reaching 0.75 cm^3 K mol^{-1} at 2.90 K. Under the action of LF, the $^4I_{9/2}$ state splits into 5 Kramer doublets, and depending on the symmetry of this field, the $m_J = \pm 9/2$ or $\pm 1/2$ states could be the ground state. Hence, the maximum magnetization value of 1.51 Nβ at 2 K is smaller than expected for a decet ground state ($M_{sat} = g_J J N\beta = 3.27$ Nβ with $J = 9/2$ and $g_J = 8/11$) (inset of Figure 5a), being however close to that observed experimentally for other magnetically isolated Nd^{3+} ions in Nd-oxamate compounds [17,32]. The reduced magnetization curves show an almost complete overlap of the curves (Figure S10a). Due to the symmetry of compound **1**, it was possible to use the Hamiltonian below (Equation (1)) to simulate the magnetic properties of this compound [33]:

$$H = \lambda LS + \Delta\left[L_z^2 - L^2\right] + (-\kappa L + 2S)\beta H \quad (1)$$

where λ is the spin-orbit coupling parameter; Δ, energy gap between the M_L values; κ = orbital reduction parameter ($\kappa = 1$ was fixed); β is Bohr magneton; L, S and H represent the angular operator, the spin operator and the magnetic field vector, respectively. Simultaneous fitting of $\chi_M T$ vs. T and M vs. H curves using PHI software (version 3.1.6) [34] yielded the following values: $\lambda = 258.94$ cm^{-1} and $\Delta = +55.45$ cm^{-1} (Table 2). The calculated curves match the experimental data over the temperature range (solid lines in Figure 5a). The λ, Δ and ΔE (the separation between the ground and the first excited states) values are within the range observed for similar Nd^{3+} compounds (see Table 2) [33,35]. Simulations with negative axial distortion values were performed, showing a very slight decrease in the $\chi_M T$ product with cooling, which is inconsistent with the fact that compound **1** shows an $\chi_M T$ product at low temperatures close to 0.8 cm^3 K mol^{-1}, a value expected for a ground state with $m_J = \pm 1/2$ [35].

For isotropic gadolinium(III) complex **2**, the $\chi_M T$ vs. T curve follows a Curie law over an extensive temperature range, with a $\chi_M T$ value at room temperature of 7.67 cm^3 K mol^{-1}, slightly lower than the expected value for a Gd^{3+} ion with a $^8S_{7/2}$ ground state (7.88 cm^3 K mol^{-1} with $S = 7/2$ and $g = 2$) (Figure 5b). Upon cooling, the $\chi_M T$ product remains constant until approximately 13 K, after which a decrease is observed, reaching a value of 6.32 cm^3 K mol^{-1} at 2.0 K. The slight decrease in the $\chi_M T$ at low temperatures may occur due to weak intermolecular antiferromagnetic interactions. The reduced magnetization curves show an almost complete overlap (inset of Figure S10b). A saturation effect is observed with a magnetization value of 7.05 Nβ at 50 kOe, close to the expected value for isotropic Gd^{3+} ions ($M_{sat} = 7$ Nβ with $S = 7/2$ and $g = 2$). Using the PHI software, simultaneous fitting of the $\chi_M T$ vs. T and M vs. H was performed through a mean-field model considering an effective intermolecular interaction (zJ) between the Gd^{3+} ions. The calculated curves match the experimental data over the temperature range and, particularly, the decrease in $\chi_M T$ at low temperatures (solid lines in Figure 5a). The calculated value of $g = 2.0$ agrees with the expected value for this isotropic ion ($g = 2.0$). The calculated zJ value of -0.01 cm^{-1} is consistent with a small but non-negligible interaction, likely a dipolar interaction.

For terbium(III) complex **3**, $\chi_M T$ is 11.65 cm^3 K mol^{-1} at room temperature and gradually decreases until around 50 K, when the decrease becomes steeper, reaching 6.89 cm^3 K mol^{-1} at 2.0 K (Figure 5c). The expected $\chi_M T$ value for Tb^{3+} ions with a $^7F_6$ ground state is well-separated from the first $^7F_5$ excited state in a free-ion approximation is 11.88 cm^3 K mol^{-1} ($S = 3$, $J = 6$ and $g_J = 3/2$). The decrease in $\chi_M T$ upon cooling from room temperature is due to the depopulation of higher energy m_J states, resulting from the LF splitting. Hence, the reduced magnetization curves do not overlap (inset of Figure S10) but show apparent saturation with a maximum value of 4.76 Nβ at 2.0 K and 5.0 T. This value is smaller than expected for a tredecet ground state (M_{sat} = 9 Nβ with $J = 6$ and $g_J = 3/2$) (inset of Figure 5c). The experimental magnetic data were fitted using the previously presented Hamiltonian (Equation (1)). This fit showed good agreement between the experimental and theoretical data. The calculated λ value of -387.29 cm^{-1} is consistent with related terbium(III) compounds [33]. The calculated Δ parameter of -48.64 cm^{-1} is within the range observed in similar terbium(III) compounds and has a negative sign, confirming an $m_J = \pm 6$ (ground state). To improve the fit at low temperatures, a zJ component was added, yielding a value of -0.023 cm^{-1}, like that observed for **2**.

For dysprosium(III) complex **4**, a decrease in the $\chi_M T$ is 14.16 cm^3 K mol^{-1} at room temperature. According to the free ion approximation model, this value is very close to the expected one for a Dy^{3+} ion with a $^6H_{15/2}$ ground state, well-separated from the first $^6H_{13/2}$ excited state (14.17 cm^3 K mol^{-1} with $J = 15/2$ and $g_J = 4/3$). As the sample is cooled, a gradual decrease in the $\chi_M T$ is observed (Figure 5d), reaching 10.00 cm^3 K mol^{-1} at approximately 13 K. This smooth decrease in the $\chi_M T$ product is characteristic of the depopulation of higher energy m_J states resulting from the LF splitting. Below 10 K, a more pronounced decrease is observed; however, in this case, this effect may be related to weak intermolecular antiferromagnetic interactions, already observed and quantified in compounds **2** and **3**. The reduced magnetization curves do not overlap (Figure S10), and no saturation effects are observed, even at the lowest temperature and highest field. The maximum M value of 5.3 Nβ at 2.0 K and 7.0 T is smaller than expected for a hexadecet ground state (M_{sat} = 10 Nβ with $J = 15/2$ and $g_J = 4/3$).

Based on the crystal structure and the formal charge of the atoms in the structure, it is possible to determine the easy magnetization axis in compounds containing dysprosium(III) ions and its energy barrier through the electrostatic model (Table S10) [36]. In the case of **4**, this axis lies in the xz plane (crystallographic ac plane), intersecting these axes at an angle close to 45 degrees (Figure 6a). By observing the crystal packing of **4**, it can be noted that there is an alternation in the directions of the anisotropy axis, which justifies the presence of antiferromagnetic interactions in this compound and possibly in the others presented in this contribution (Figure 6b). However, despite the simplicity of providing the easy axis of magnetization using the Magellan software [36], high-level quantum chemical calculations such as Complete Active Space Self-Consistent Field (CASSCF calculations) could give further insights into the effects of crystal field, the nature of the Dy–O bond, and the covalent factors influencing the magnetic properties of these compounds.

3.3. Dynamic Magnetic Properties

Dynamic alternating current (ac) magnetic properties for **1**–**4** are presented in Figures 7–10, respectively, in the form of the χ_M' and χ_M'' vs. ν curves (χ_M' and χ_M'' being the in-phase and out-of-phase ac magnetic susceptibilities per mononuclear unit, and ν is the frequency). Table 3 summarizes all magnetic ac data for **1**–**4** obtained using CC-FIT2 software v5.8.0 [37,38].

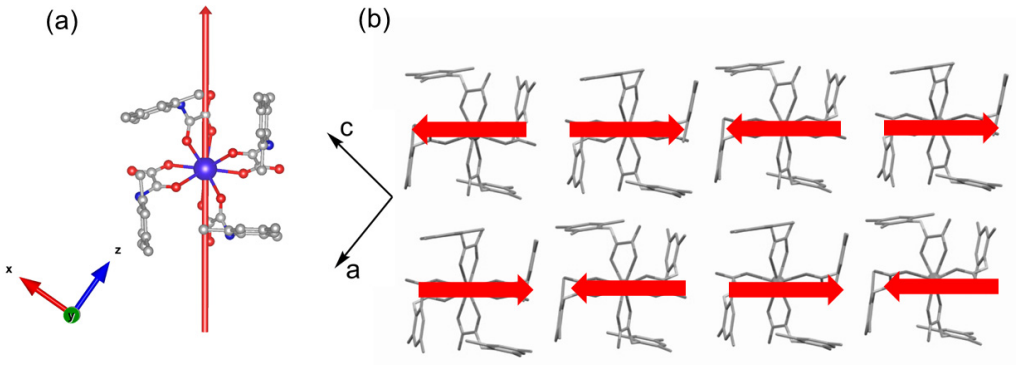

Figure 6. (**a**) Representation of the easy magnetization axis of dysprosium(III) complex **4** as a red arrow in each single-ion magnet (color code: Dy in violet, N in blue, oxygen in red, carbon in grey). (**b**) The easy magnetization axis is represented by red arrows in the crystal packing of **4** along the crystallographic *ac* direction. For clarity, the hydrogen atoms, solvent molecules and counterions were omitted.

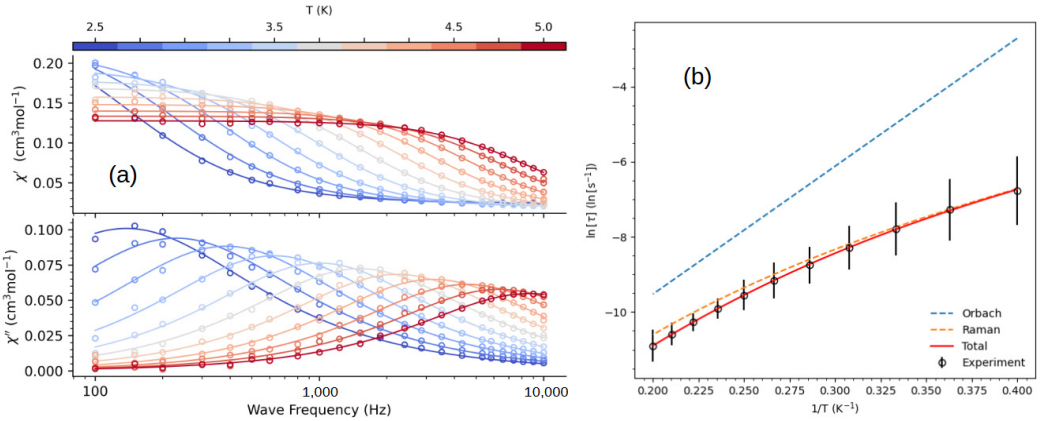

Figure 7. (**a**) χ_M' and χ_M'' vs. ν curves of **1** under 1.0 kOe dc magnetic field. (**b**) Arrhenius plot of **1** under 1.0 kOe dc magnetic field. Solid lines represent fits to the data (see text).

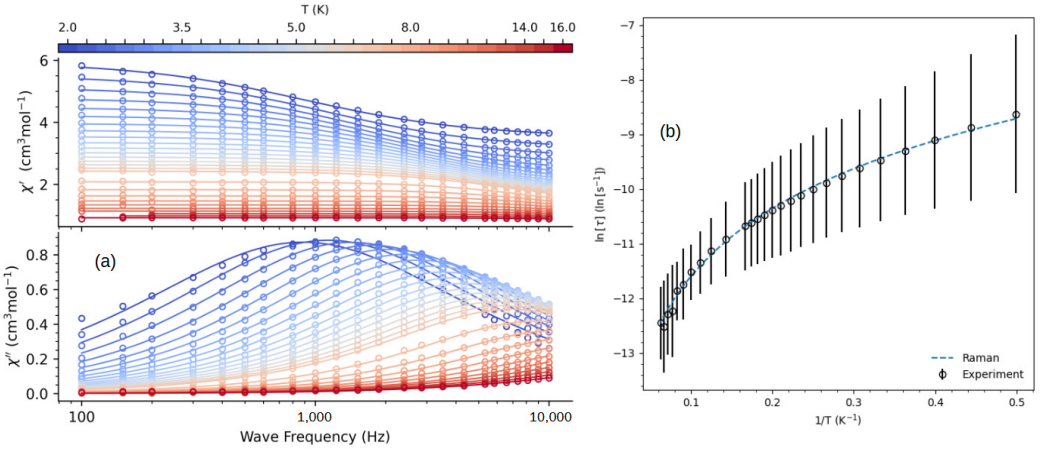

Figure 8. (**a**) χ_M' and χ_M'' vs. ν curves of **2** under 1.0 kOe dc magnetic field. (**b**) Arrhenius plot of **2** under a 1.0 kOe dc magnetic field. Solid lines represent fits to the data (see text).

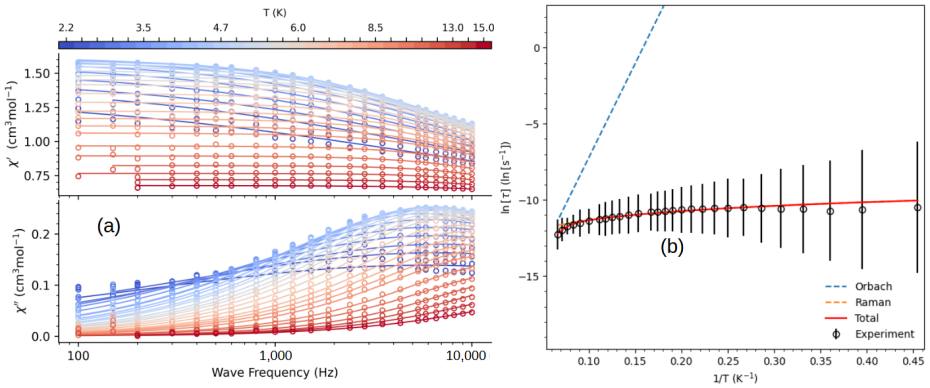

Figure 9. (**a**) $\chi_M{}'$ and $\chi_M{}''$ vs. ν curves of **3** under 5.0 kOe dc magnetic field. (**b**) Arrhenius plot of **3** under 5.0 kOe dc magnetic field. Solid lines represent fits to the data (see text).

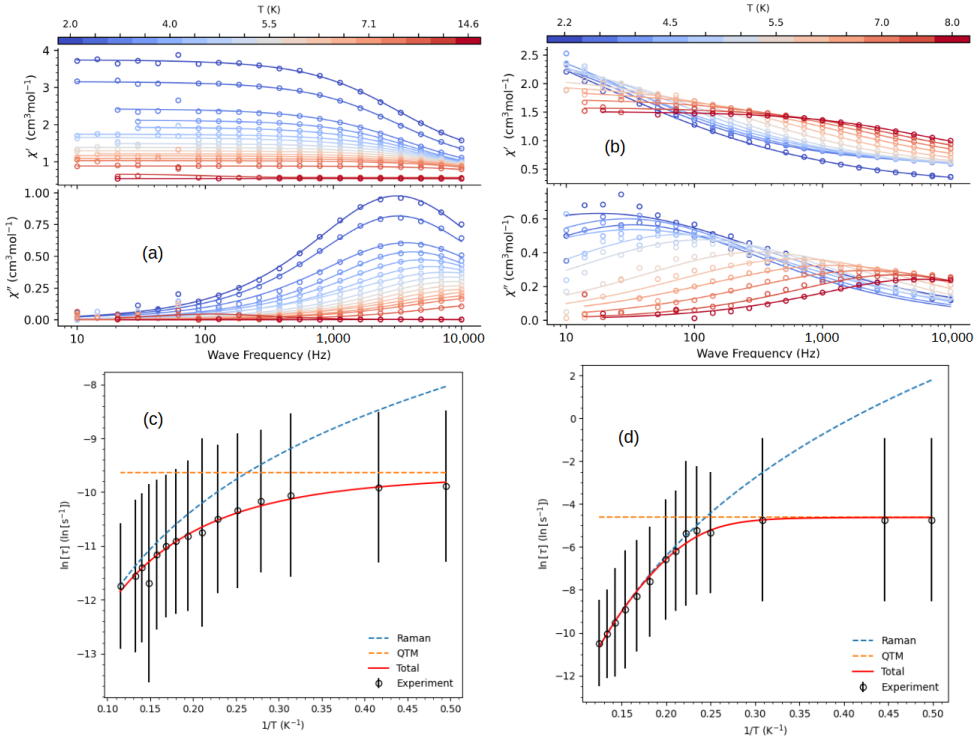

Figure 10. $\chi_M{}'$ and $\chi_M{}''$ vs. ν curves of compound **4** under (**a**) zero dc magnetic field and (**b**) 1.0 kOe dc magnetic field. Arrhenius plots of **4** (**c**) under zero dc field and (**d**) 1.0 kOe dc field. Solid lines represent fits to the data (see text).

Under zero dc field, frequency-dependent $\chi_M{}'$ and $\chi_M{}''$ signals were observed in **4** with $\chi_M{}''$ maxima at temperatures ranging from 2 to 6 K, indicating the occurrence of slow magnetic relaxation, as shown in Figure 10a. Upon applying a static dc field of 1.0 kOe, the temperature at which $\chi_M{}''$ appears shifts to 8 K, as illustrated in Figure 10b. The $\chi_M{}'$ and $\chi_M{}''$ vs. ν curves were fitted to the generalized Debye model [39] to extract temperature-dependent relaxation times (τ). The resulting τ versus T^{-1} (so-called Arrhenius plots) are shown in Figure 10c for a zero-dc field and Figure 10d for a dc field of 1.0 kOe. All parameters determined from these fitting processes, such as the isothermal and thermal susceptibility, χ_S and χ_T, relaxation time and its distribution, τ and α, are summarized in Tables S11 and S12. The distribution of relaxation times is relatively narrow, with α close to 0.2 at zero dc field (Table S11). For a dc field of 1.0 kOe, α approaches the value of 0.5 at a low temperature (Table S12).

Table 3. Selected ac magneto-structural data for some mononuclear oxamate-containing Ln-SMMs and Ln-SIMs.

Compound	Ln···Ln [a] (Å)	Ln	CN [b]	Sym. [c]	H_{DC} (kOe)	U_{eff}/k_B (K)	τ_0 (s)	τ_{QTM} (s)	C (s^{-1} K^{-1})	n	A (s^{-1} K^{-n})	Process	Ref.
1	11.466	Nd	9	C_s	1.0	34(2)	$8.0(9) \times 10^{-8}$		4.87(3)	5.6(2)		Orbach + Raman	This work
2	11.158	Gd	9	C_{4v}	1.0				1746(12)	1.80(2)		Bottleneck	This work
3	11.128	Tb	9	C_{4v}	5.0	21(5) × 10	$1.2(5) \times 10^{-11}$				889(3) × 10	Orbach + Raman + Direct	This work
4	11.179	Dy	9	C_{4v}	0			$6.6(2) \times 10^{-5}$	520(32)	2.5(3)		Raman + QTM	This work
					1.0			$9.06(7) \times 10^{-3}$	$3.2(3) \times 10^{-4}$	9.0(3)		Raman + QTM	This work
n-$Bu_4N[Nd(L1)_4(DMSO)]_2 \cdot 3H_2O$	11.169	Nd	9	D_{3h}	1.0	16.7(5) [d]	$1(3) \times 10^{-4}$		0.005(4)	4.7(2)		Orbach + Raman	[19]
n-$Bu_4N[Nd(L2)_4(DMSO)]_2 \cdot 2H_2O$	11.228	Nd	9	D_{3h}	1.0	4.9(1) [d]	$9.5(7) \times 10^{-4}$		0.03(4)	11(1)		Orbach + Raman	[19]
$[Nd(L3)_3(DMSO)_2]_n$	8.8709(3)	Nd	9	C_{4v}	1.0	42.7(2)	$2.3(1) \times 10^{-8}$		26.7(1)	3.9(1)		Orbach + Raman	[34]
$Na[Gd(L4)_4(H_2O)]_2 \cdot 2H_2O$	7.3014(7)	Gd	9	C_{4v}	1.0	13(1)	6.1×10^{-6}		$2(1) \times 10^{-5}$	3	2.9(1)	Direct + Raman	[14]
n-$Bu_4N[Gd(L1)_4(DMSO)]_2 \cdot 2H_2O$	11.0272(6)	Gd	9	D_{3h}	1.0				$4.5(5) \times 10^3$	1.6(1)		Bottleneck	[18]
n-$Bu_4N[Gd(L2)_4(DMSO)]_2 \cdot 3H_2O$	10.6005(7)	Gd	9	D_{3h}	1.0				$1.1(1) \times 10^3$	1.8(1)		Bottleneck	[18]
$\{Gd_2(L5)_3(H_2O)_5 \cdot H_2O\}_n$	10.163(3)	Gd	8	T_d	1.0	3.27 [d]	5.4×10^{-6}					Orbach	[35]
$[Gd(L6)_3(DMSO)_2]_n \cdot nH_2O$	6.702	Gd	9	C_{4v}	1.0					1.9(2)	125.89	Bottleneck	[17]
	6.702	Gd	9	C_{4v}	2.5					2.1(1)	39.81	Bottleneck	[17]
$Me_4N[Dy(L7)_4]_2CH_3CN$	9.032(1)	Dy	8	D_{2d}	1.0	93.66 [d]	$2.88(8) \times 10^{-10}$					Orbach	[13]
$Na[Dy(L4)_4(H_2O)]_2 \cdot 2H_2O$	7.2881(4)	Dy	9	C_{4v}	1.0	16(1)	$1.4(9) \times 10^{-8}$		2(5)	9		Orbach + Raman	[14]
n-$Bu_4N[Tb(L1)_4(DMSO)]_2 \cdot 2H_2O$	10.9998(5)	Tb	9	D_{3h}	2.0			2.04×10^{-4}	20(6)	3.5(2)		Raman + QTM	[18]
n-$Bu_4N[Tb(L2)_4(DMSO)]_2 \cdot 3H_2O$	10.6121(2)	Tb	9	D_{3h}	1.0				6.6(9)	3.8(2)	$13.7(3) \times 10^1$	Raman + direct	[18]

Ligand abbreviations: L1 = *N*-4-(chorophenyl)oxamate; L2 = *N*-4-(fluorophenyl)oxamate; L3 = *N*-(4-methylphenyl)oxamate; L4 = *N*-4-(hydroxyphenyl)oxamate; L5 = *N*-(4-carboxyphenyl)oxamic acid; L6 = *N*-(phenyl)oxamate; L7 = *N*-(2,6-dimethylphenyl)oxamic acid. [a] Shortest intermolecular Ln···Ln distance. [b] Coordination number of the Ln ion. [c] Symmetry around the Ln ion according to the continuous shape measurements [30]. [d] Original values were converted from cm^{-1} to K for comparative purposes.

Relaxation processes of Dy-based SIMs have been analyzed, considering a combination of Orbach relaxation process at higher temperatures, Raman at intermediate temperatures and quantum tunneling of magnetization (QTM) at low temperatures [5]. Consequently, the data obtained for **4** were analyzed using Equation (2) below.

$$\tau^{-1} = CT^{n} + {\tau_0}^{-1} \exp(-U_{eff}/k_B T) + {\tau_{QTM}}^{-1} \quad (2)$$

The first term of the right side of Equation (2) represents the Raman process, the second term represents the Orbach process and the third term represents the QTM relaxation processes. A combination of Raman and QTM processes better described the data. For the zero dc field, resulting in the best-fit parameters as C = 520(32) s^{-1} K^{-n}, n = 2.5(3) and τ_{QTM} = 6.6(2) × 10^{-5} s. Under a 1.0 kOe dc applied field, the best-fit parameters were C = 3.2(3) × 10^{-4} s^{-1} K^{-n}, n = 9.0(3) and τ_{QTM} = 9.8(1) × 10^{-3} s. These parameter values are consistent with the energy barrier observed for Dy^{3+} ions with the same coordination number [40].

Unlike **4**, compounds **1**–**3** show no χ_M'' signal under zero dc magnetic field above 2.0 K, indicating fast relaxation processes through QTM. Applying a static dc field, however, induces slow magnetic relaxation in **1**–**3**, as shown in Figures 7a, 8a and 9a. Relaxation times for **1**–**3** were determined by fitting the χ_M' and χ_M'' vs. ν curves to the generalized Debye model [39]. The resulting Arrhenius plots are shown in Figures 7b, 8b and 9b, respectively. The determined values of χ_S and χ_T, τ and α for **1**–**3** are summarized in Tables S13–S16.

For **1**, the relaxation time was accurately determined within the 2–5 K temperature range. The distribution of relaxation times was narrow, with α close to 0.1 (Table S12). The Arrhenius plot was fitted considering Raman and Orbach processes, as reported previously [41,42]. The best fit parameters are U_{eff} = 34(2) K, τ_0 = 8.0(9) × 10^{-8} s, C = 4.87(3) s^{-1} K^{-n}, n = 5.6(2). These results are consistent with values reported by other authors for Nd-based molecular material [41,42]. The direct process ($\tau^{-1} = A\,H^{n1}T$) was ruled out for this complex as the field-dependent results deviated significantly from the typically exponential values (n_1 = 2–4) described by other researchers, as shown in Figure S11 [43].

For **2**, under an applied field of 1.0 kOe, the SMR was observed within the temperature range of 2–16 K, as shown in Figure 8a. The distribution of relaxation times is narrow, reaching a maximum value at 2 K with α close to 0.2 (see Table S14). Therefore, the Arrhenius plot of **2** (Figure 8b) was fitted by considering the Raman process, resulting in the following values: C = 1746(12) s^{-1} K^{-n} and n = 1.80(2). These values suggest that the magnetic relaxation mechanism in the Gd^{3+} compound is associated with the bottleneck effect, as expected for n values near 2 [12–16]. This is consistent with findings reported by other authors for field-induced Gd-based SIMs [12,13,15,16,44].

Although compound **3** showed frequency dependence in out-of-phase magnetic susceptibility under a 1.0 kOe magnetic field (Figure S12, Table S15), peaks in the χ_M'' vs. ν curves were only observed under a 5.0 kOe dc magnetic field, as shown in Figure 9a. The distribution of relaxation times is broad at low temperatures (α value close to 0.6 at 2 K), suggesting multiple relaxation processes occurring within this temperature range. Above 5.0 K, the distribution is relatively narrow, where α begins to decrease from a value close to 0.2, as shown in Table S16. The Arrhenius plot of **3** (Figure 9b) was fitted considering the Orbach, Raman, Direct and QTM processes [12,39]. The best fit was obtained considering the Orbach and Direct processes, resulting in U_{eff} = 21(5) × 10 K, τ_0 = 1.2(5) × 10^{-11} s, A = 889(3) × 10 s^{-1} K^{-1}. These values are consistent with findings reported by other authors for field-induced slow magnetic relaxation for Tb-based SIMs [45].

Table 3 compares the results of mononuclear complexes and coordination polymers based on oxamate containing Kramer Ln^{III} ions (Ln = Nd, Dy, and Gd) and non-Kramer Ln^{III} ions (Tb) in low coordinate that exhibited SMR phenomena. Additionally, it is worth emphasizing that an ideal point group symmetry such as $C_{\infty v}$, D_{4d}, S_8, D_{5h}, D_{6d} and $D_{\infty h}$ could suppress the unwanted QTM process [5]. Once these precise geometries are unlikely to be realized in molecular complexes in general, taking into account the oxamate derivatives (Table 3). The suppression of QTM phenomena can be achieved by diluting

the paramagnetic complexes within an isostructural diamagnetic matrix, which can reduce the dipolar interactions and/or by applying an external static dc magnetic field. Only **4** exhibits the SMR at zero dc field, while all other oxamate compounds synthesized up to date (Table 3) behave as field-induced SMMs. In the case of **4**, the Raman and QTM mechanisms are dominant. Dysprosium(III) ions are anisotropic; thus, the observation of the SRM phenomena is expected for Dy-complexes. The fitting results show that the QTM occurs for Dy^{3+} complexes in some extensions, even with an application of an H_{dc} of 1.0 kOe, which is not strong enough to suppress the QTM. Additionally, the extension of the QTM in this complex does not preclude the observation of SMR phenomena in **4**. The energy of the barrier for spin reversal was obtained in the Magellan software (Table S10). The minimum energy of the crystalline structure was calculated as -187 cm^{-1}, while the minimum energy barrier for the spin reversal was determined as +22.9 cm^{-1}. This value is very close to the experimental one determined through the fits of magnetic data (+23.63 cm^{-1} or 34 K, see Table 3), indicating that the model employed describes the energy values with reasonable precision [36].

Neodymium(III)–oxamate compounds exhibited the Orbach and Raman mechanism that accounts for the SMR phenomena, as observed for all Nd-complexes of Table 3, even with different local symmetries around the metal ion and ligands containing donor [*N*-4-(methyl)oxamate] or electron-withdrawing groups [*N*-4-(chlorophenyl)oxamate and (*N*-4-(fluorophenyl)oxamate)]. Comparing the value of the energy barrier of **1** and the other compounds of Table 3, the energy barrier values are higher for complexes containing only oxamate-donor ligands. Comparing the energy barrier of **1** and **4** with $H_{dc} \neq 0$, due to the higher anisotropy and m_J states of **4**, a higher energy barrier for **4** is achieved.

In contrast to Nd^{3+}, Tb^{3+} and Dy^{3+} ions, Gd^{3+} ions are isotropic, and the SMR is not expected for such complexes. However, a very low magnetic anisotropy with a low value of zero-field splitting (D~0.1 cm^{-1}) can be found experimentally for gadolinium(III) compounds. With the application of a magnetic field, the asymmetric surrounding of the gadolinium(III) ions can increase the D value parameter, which can cause a split in the ground state doublet ($m_s = \pm 7/2$) and, consequently, the admixture with the ground and some excited states. Consequently, the SMR cannot be explained in many cases by considering the conventional over-barrier mechanisms or suppression of tunneling, which occurs with anisotropic systems. When the SMR phenomena are observed in Gd^{3+} complexes, the interaction between the magnetic ion and its environment should be considered. Focusing on the case of nine-coordinate gadolinium(III) ions, the phonon bottleneck mechanism is predominant, observed for **2** and the other three compounds from Table 3, with D_{3h} and C_4 symmetries. The phonon bottleneck effect occurs when the dc field is applied, suppressing QTM relaxation. It arises when the energy from lattice modes generated by relaxing spins, transitioning from excited to ground states, cannot be dissipated into the thermal reservoir at a sufficiently fast rate. However, for $\{Gd_2(L5)_3(H_2O)_5 \cdot H_2O\}_n$ (L5 = *N*-(4-carboxyphenyl)oxamic acid), the mechanism involved is Orbach, while for $Na[Gd(L4)_4(H_2O)]_2 \cdot 2H_2O$ (L4 = *N*-4-(hydroxyphenyl)oxamate) it is attributable to direct and Raman processes.

In the case of terbium(III) complex **3**, a non-Kramer ion, the SMR is not expected without an external magnetic field [5]. Moreover, the application of a small external magnetic field can induce SMR; therefore, most terbium(III) complexes exhibit behavior characteristic of field-induced single-molecule magnets (SMMs) or field-induced single-ion magnets (SIMs). Besides the external field, an ideal molecular symmetry causing appropriate local symmetry around the metal centre can also cause SMR in mononuclear Tb compounds. In the case of **4**, the fit of the Arrhenius plot reveals that the magnetic dynamics follow the power law corresponding to Orbach and direct processes. Comparing this compound with other Tb–oxamate complexes, it is noticed that **3** has the highest energy barrier. Probably, this result is associated with the higher value of the magnetic field to promote the SMR.

4. Conclusions

In summary, we synthesized four lanthanide(III) complexes with the ligand *N*-(2,4,6-trimethylphenyl)oxamate featuring a calixarene-like structure. The gadolinium(III), terbium(III) and dysprosium(III) complexes are nine-coordinated and isostructural, with CSAPR-9 symmetry, while the neodymium(III) complex, with a nine-coordinate (MFF-9) geometry, is not. The dysprosium(III) complex **4** is the first example of an oxamate-based Ln-SIM without applying a dc field. The neodymium(III), gadolinium(III) and terbium(III) complexes behave instead as field-induced Ln-SIMs. These results suggest that by improving the geometry around the metal center and using oblate ions, it would be possible to improve the performance of oxamate-based Ln SIMs, reaching higher temperatures and higher energy barriers for spin reversal.

Supplementary Materials: The following supporting information can be downloaded at: https://www.mdpi.com/article/10.3390/magnetochemistry10120103/s1, Figure S1: FTIR spectra of **1**–**4**; Figure S2: TG (solid line) and DTA (dashed line) curves for **1** in synthetic air atmosphere; Figure S3: TG (solid line) and DTA (dashed line) curves for **2** in synthetic air atmosphere; Figure S4: TG (solid line) and DTA (dashed line) curves for **3** in synthetic air atmosphere; Figure S5: TG (solid line) and DTA (dashed line) curves for **3** in synthetic air atmosphere; Figure S6: Experimental and simulated PXRD patterns of **1**; Figure S7: Experimental and simulated PXRD patterns of **2**; Figure S8: Experimental and simulated PXRD patterns of **3**; Figure S9: Experimental and simulated PXRD patterns of **4**; Figure S10: Reduced magnetization curves of **1**–**4** (H_{dc} = 0.2 kOe). Figure S11: Field dependence of the direct process coefficient for **1**. (a) Fitted considering Orbach + Direct processes, and (b) Raman + Direct processes. Figure S12: In-phase and out-of-phase magnetic susceptibilities of **3** were obtained for a 1.0 kOe dc magnetic field. Table S1: Selected bond lengths (Å) and angles (°) for complex **1**. Table S2: Selected bond lengths (Å) and angles (°) for complex **2**. Table S3: Selected bond lengths (Å) and angles (°) for complex **3**. Table S4: Selected bond lengths (Å) and angles (°) for complex **4**. Table S5: Hydrogen bonds for complex **1** [Å and °]. Table S6: Hydrogen bonds for complex **2** [Å and °]. Table S7: Hydrogen bonds for complex **3** [Å and °]. Table S8: Hydrogen bonds for complex **4** [Å and °]. Table S9: CShM calculations of the coordination environment at lanthanide(III) ion in all complexes of LnL_9 coordination sphere of **1**–**4** [30]. Table S10: Energy values were obtained through the Magellan software [36]. Table S11: Debye parameters of **4** from the AC susceptibility data measured with zero dc magnetic field. Table S12: Debye parameters of **4** from the ac susceptibility data were measured with a 1.0 kOe dc magnetic field. Table S13: Debye parameters of **1** from the ac susceptibility data were measured with a 1.0 kOe dc magnetic field. Table S14: Debye parameters of **2** from the ac susceptibility data were measured with a 1.0 kOe dc magnetic field. Table S15: Debye parameters of **3** from the ac susceptibility data were measured with a 1.0 kOe dc magnetic field. Table S16: Debye parameters of **3** from the ac susceptibility data were measured with a 5.0 kOe dc magnetic field.

Author Contributions: Investigation and methodology, writing original draft, T.T.d.C.; investigation, J.H.d.A.-N. and M.E.A.; validation, writing review and editing, F.T.M.; investigation, writing original draft, E.F.P., D.L.M., W.C.N. and N.M.; resources, project administration, writing—review and editing, F.L., M.J.; conceptualization, funding acquisition, supervising, writing review and editing, C.L.M.P. All authors have read and agreed to the published version of the manuscript.

Funding: This research was funded by Conselho Nacional de Desenvolvimento Científico e Tecnológico (CNPq), the Coordenação de Aperfeiçoamento de Pessoal de Nível Superior (CAPES), the Bioanalytical Facility NEPS-DQ/UFMG, the Fundação de Amparo à Pesquisa do Estado de Minas Gerais, the Fundo de Amparo à Pesquisa do Estado do Rio de Janeiro, the Spanish MINECO (Project PID201935-GB-I00) and Unidad de Excelencia Maria de Maeztu CEX2019-000919 for financial support.

Data Availability Statement: All data of this manuscript are available in the Supplementary Materials. Crystal structures were deposited with the Cambridge Crystallographic Data Center with numbers 2380352 (**1**), 2380353 (**2**), 2380351 (**3**) and 2380354 (**4**) and are available under request.

Conflicts of Interest: The authors declare no conflicts of interest to disclose.

References

1. Bartolomé, E.; Arauzo, A.; Luzón, J.; Bartolomé, J.; Bartolomé, F. Magnetic Relaxation of Lanthanide-Based Molecular Magnets. In *Handbook of Magnetic Materials*; North-Holland: Amsterdam, The Netherlands, 2017; Volume 26, pp. 1–289. [CrossRef]
2. Ferrando-Soria, J.; Vallejo, J.; Castellano, M.; Martínez-Lillo, J.; Pardo, E.; Cano, J.; Castro, I.; Lloret, F.; Ruiz-García, R.; Julve, M. Molecular Magnetism, Quo Vadis? A Historical Perspective from a Coordination Chemist Viewpoint. *Coord. Chem. Rev.* **2017**, *339*, 17–103. [CrossRef]
3. Rabelo, R.; Stiriba, S.E.; Cangussu, D.; Pereira, C.L.M.; Moliner, N.; Ruiz-García, R.; Cano, J.; Faus, J.; Journaux, Y.; Julve, M. When Molecular Magnetism Meets Supramolecular Chemistry: Multifunctional and Multiresponsive Dicopper(Ii) Metallacyclophanes as Proof-of-Concept for Single-Molecule Spintronics and Quantum Computing Technologies? *Magnetochemistry* **2020**, *6*, 69. [CrossRef]
4. Ishikawa, N. Simultaneous Determination of Ligand-Field Parameters of Isostructural Lanthanide Complexes by Multidimensional Optimization. *J. Phys. Chem. A* **2003**, *107*, 5831–5835. [CrossRef]
5. Parmar, V.S.; Mills, D.P.; Winpenny, R.E.P. Mononuclear Dysprosium Alkoxide and Aryloxide Single-Molecule Magnets. *Chem. Eur. J.* **2021**, *27*, 7625–7645. [CrossRef]
6. Blagg, R.J.; Ungur, L.; Tuna, F.; Speak, J.; Comar, P.; Collison, D.; Wernsdorfer, W.; McInnes, E.J.L.; Chibotaru, L.F.; Winpenny, R.E.P. Magnetic Relaxation Pathways in Lanthanide Single-Molecule Magnets. *Nat. Chem.* **2013**, *5*, 673–678. [CrossRef]
7. Rinehart, J.D.; Long, J.R. Exploiting Single-Ion Anisotropy in the Design of f-Element Single-Molecule Magnets. *Chem. Sci.* **2011**, *2*, 2078. [CrossRef]
8. Zheng, Y.Z.; Zhou, G.J.; Zheng, Z.; Winpenny, R.E.P. Molecule-Based Magnetic Coolers. *Chem. Soc. Rev.* **2014**, *43*, 1462–1475. [CrossRef]
9. Bünzli, J.-C.G.; Chauvin, A.-S. Lanthanides in Solar Energy Conversion. In *Handbook on the Physics and Chemistry of Rare Earths*; North-Holland: Amsterdam, The Netherlands, 2014; Volume 44, pp. 169–281. [CrossRef]
10. Bünzli, J.C.G. On the Design of Highly Luminescent Lanthanide Complexes. *Coord. Chem. Rev.* **2015**, *293–294*, 19–47. [CrossRef]
11. Fortea-Pérez, F.R.; Vallejo, J.; Julve, M.; Lloret, F.; De Munno, G.; Armentano, D.; Pardo, E. Slow Magnetic Relaxation in a Hydrogen-Bonded 2D Array of Mononuclear Dysprosium(III) Oxamates. *Inorg. Chem.* **2013**, *52*, 4777–4779. [CrossRef]
12. da Cunha, T.T.; Barbosa, V.M.M.; Oliveira, W.X.C.; Pinheiro, C.B.; Pedroso, E.F.; Nunes, W.C.; Pereira, C.L.M. Slow Magnetic Relaxation in Mononuclear Gadolinium(III) and Dysprosium(III) Oxamato Complexes. *Polyhedron* **2019**, *169*, 102–113. [CrossRef]
13. Mayans, J.; Escuer, A. Correlating the Axial Zero Field Splitting with the Slow Magnetic Relaxation in Gd^{III} SIMs. *Chem. Commun.* **2021**, *57*, 721–724. [CrossRef] [PubMed]
14. da Cunha, T.T.; Barbosa, V.M.M.; Oliveira, W.X.C.; Pedroso, E.F.; García, D.M.A.; Nunes, W.C.; Pereira, C.L.M. Field-Induced Slow Magnetic Relaxation of a Six-Coordinate Mononuclear Manganese(II) and Cobalt(II) Oxamate Complexes. *Inorg. Chem.* **2020**, *59*, 12983–12987. [CrossRef] [PubMed]
15. da Silveira, C.O.C.; Oliveira, W.X.C.; da Silva Júnior, E.N.; Alvarenga, M.E.; Martins, F.T.; Gatto, C.C.; Pinheiro, C.B.; Pedroso, E.F.; Silva, J.P.O.; Marques, L.F.; et al. Photoluminescence and Magnetic Properties of Isostructural Europium(III), Gadolinium(III) and Terbium(III) Oxamate-Based Coordination Polymers. *Dalton Trans.* **2024**, *53*, 14995–15009. [CrossRef] [PubMed]
16. Vaz, R.C.A.; Esteves, I.O.; Oliveira, W.X.C.; Honorato, J.; Martins, F.T.; Marques, L.F.; dos Santos, G.L.; Freire, R.O.; Jesus, L.T.; Pedroso, E.F.; et al. Mononuclear Lanthanide(III)-Oxamate Complexes as New Photoluminescent Field-Induced Single-Molecule Magnets: Solid-State Photophysical and Magnetic Properties. *Dalton Trans.* **2020**, *49*, 16106–16124. [CrossRef]
17. Vaz, R.C.A.; Esteves, I.O.; Oliveira, W.X.C.; Honorato, J.; Martins, F.T.; da Silva Júnior, E.N.; de C. A. Valente, D.; Cardozo, T.M.; Horta, B.A.C.; Mariano, D.L.; et al. Lanthanide(III)-Oxamato Complexes Containing Nd^{3+} and Ho^{3+}: Crystal Structures, Magnetic Properties, and Ab Initio Calculations. *CrystEngComm* **2022**, *24*, 6628–6641. [CrossRef]
18. Wang, J.; Jing, Y.; Cui, M.; Lu, Y.; Ouyang, Z.; Shao, C.; Wang, Z.; Song, Y. Spin Qubit in a 2D Gd^{III} Na^{I} -Based Oxamato Supramolecular Coordination Framework. *Chem. Eur. J.* **2023**, *29*, e202301771. [CrossRef]
19. Pardo, E.; Ruiz-García, R.; Lloret, F.; Faus, J.; Julve, M.; Journaux, Y.; Delgado, F.; Ruiz-Pérez, C. Cobalt(II)-Copper(II) Bimetallic Chains as a New Class of Single-Chain Magnets. *Adv. Mater.* **2004**, *16*, 1597–1600. [CrossRef]
20. Araujo Junior, C.R.; Oliveira, W.X.C.; Pinheiro, C.B.; Pedroso, E.F.; Nunes, W.C.; de Almeida, A.A.; Knobel, M.; Julve, M.; Pereira, C.L.M. Crystal Structure and Cryomagnetic Study of a Mononuclear Erbium(III) Oxamate Inclusion Complex. *Acta Crystallogr. C Struct. Chem.* **2024**, *C80*, 349–356. [CrossRef]
21. Macrae, C.F.; Sovago, I.; Cottrell, S.J.; Galek, P.T.A.; McCabe, P.; Pidcock, E.; Platings, M.; Shields, G.P.; Stevens, J.S.; Towler, M.; et al. Mercury 4.0: From Visualization to Analysis, Design and Prediction. *J. Appl. Crystallogr.* **2020**, *53*, 226–235. [CrossRef]
22. Sheldrick, G.M. A Short History of *SHELX*. *Acta. Crystallogr. A* **2008**, *64*, 112–122. [CrossRef]
23. Dolomanov, O.V.; Bourhis, L.J.; Gildea, R.J.; Howard, J.A.K.; Puschmann, H. *OLEX2*: A Complete Structure Solution, Refinement and Analysis Program. *J. Appl. Crystallogr.* **2009**, *42*, 339–341. [CrossRef]
24. Rigaku, O.D. *CrysAlis PRO*; Rigaku Corporation: Oxford, UK, 2018.
25. Palatinus, L.; Chapuis, G. SUPERFLIP—A Computer Program for the Solution of Crystal Structures by Charge Flipping in Arbitrary Dimensions. *J. Appl. Crystallogr.* **2007**, *40*, 786–790. [CrossRef]
26. Sheldrick, G.M. Crystal Structure Refinement with SHELXL. *Acta Crystallogr. C Struct. Chem.* **2015**, *71*, 3–8. [CrossRef]
27. Johnson, C.K. *Crystallographic Computing Techniques*; Ahmed, F., Hall, S.R., Huber, C.P., Eds.; Munksgaard: Copenhagen, Denmark, 1970; pp. 207–220.

28. Pereira, C.L.M.; Doriguetto, A.C.; Konzen, C.; Meira-Belo, L.C.; Leitão, U.A.; Fernandes, N.G.; Mascarenhas, Y.P.; Ellena, J.; Brandl, A.L.; Knobel, M.; et al. A Crystalline Phase Transition and Optical Properties in a $Co^{II}Cu^{II}$ Oxamato-Bridged Ferrimagnetic Chain. *Eur. J. Inorg. Chem.* **2005**, *2005*, 5018–5025. [CrossRef]
29. da Cunha, T.T.; da Silveira, C.O.C.; Barbosa, V.M.M.; Oliveira, W.X.C.; da Silva Júnior, E.N.; Ferreira, F.F.; Pedroso, E.F.; Pereira, C.L.M. Ferromagnetic Coupling in a Dicopper(II) Oxamate Complex Bridged by Carboxylate Groups. *CrystEngComm* **2021**, *23*, 1885–1897. [CrossRef]
30. Lunell, M.; Casanova, D.; Cirera, J.; Alemany, P.; Alvarez, S. *SHAPE*, version 2.0. 2010.
31. Etter, M.C. Encoding and Decoding Hydrogen-Bond Patterns of Organic Compounds. *Acc. Chem. Res.* **1990**, *23*, 120–126. [CrossRef]
32. Diogo, E.B.T.; da Silva Júnior, E.N.; Oliveira, W.X.C.; Stumpf, H.O.; Fabris, F.; de Almeida, A.A.; Knobel, M.; Ferreira, F.F.; Nunes, W.C.; Pedroso, E.F.; et al. Isostructural Oxamate Complexes with Visible Luminescence (Eu^{3+}) and Field-Induced Single-Molecule Magnet (Nd^{3+}). *Chem. Asian J.* **2024**, *24*, e202400887. [CrossRef]
33. de Oliveira Maciel, J.W.; Lemes, M.A.; Valdo, A.K.; Rabelo, R.; Martins, F.T.; Queiroz Maia, L.J.; de Santana, R.C.; Lloret, F.; Julve, M.; Cangussu, D. Europium(III), Terbium(III), and Gadolinium(III) Oxamato-Based Coordination Polymers: Visible Luminescence and Slow Magnetic Relaxation. *Inorg. Chem.* **2021**, *60*, 6176–6190. [CrossRef]
34. Chilton, N.F.; Anderson, R.P.; Turner, L.D.; Soncini, A.; Murray, K.S. PHI: A Powerful New Program for the Analysis of Anisotropic Monomeric and Exchange-Coupled Polynuclear d- and f-Block Complexes. *J. Comput. Chem.* **2013**, *34*, 1164–1175. [CrossRef] [PubMed]
35. Ungur, L.; Chibotaru, L.F. Computational Modelling of the Magnetic Properties of Lanthanide Compounds. In *Lanthanides and Actinides in Molecular Magnetism*; Wiley: Weinheim, Germany, 2015; pp. 153–184. [CrossRef]
36. Chilton, N.F.; Collison, D.; McInnes, E.J.L.; Winpenny, R.E.P.; Soncini, A. An Electrostatic Model for the Determination of Magnetic Anisotropy in Dysprosium Complexes. *Nat. Commun.* **2013**, *4*, 2551. [CrossRef] [PubMed]
37. Reta, D.; Chilton, N.F. Uncertainty Estimates for Magnetic Relaxation Times and Magnetic Relaxation Parameters. *Phys. Chem. Chem. Phys.* **2019**, *21*, 23567–23575. [CrossRef]
38. Blackmore, W.J.A.; Gransbury, G.K.; Evans, P.; Kragskow, J.G.C.; Mills, D.P.; Chilton, N.F. Characterisation of Magnetic Relaxation on Extremely Long Timescales. *Phys. Chem. Chem. Phys.* **2023**, *25*, 16735–16744. [CrossRef]
39. Cole, K.S.; Cole, R.H. Dispersion and Absorption in Dielectrics, I. Alternating Current Characteristics. *J. Chem. Phys.* **1941**, *9*, 341–351. [CrossRef]
40. Hu, B.; Xi, J.; Cen, P.; Guo, Y.; Ding, Y.; Qin, Y.; Zhang, Y.-Q.; Liu, X. A Mononuclear Nine-Coordinated Dy(III) Complex Exhibiting Field-Induced Single-Ion Magnetism Behaviour. *RSC Adv.* **2022**, *12*, 13992–13998. [CrossRef]
41. Wada, H.; Ooka, S.; Iwasawa, D.; Hasegawa, M.; Kajiwara, T. Slow Magnetic Relaxation of Lanthanide(III) Complexes with a Helical Ligand. *Magnetochemistry* **2016**, *2*, 43. [CrossRef]
42. Wada, H.; Ooka, S.; Yamamura, T.; Kajiwara, T. Light Lanthanide Complexes with Crown Ether and Its Aza Derivative Which Show Slow Magnetic Relaxation Behaviors. *Inorg. Chem.* **2017**, *56*, 147–155. [CrossRef]
43. Liddle, S.T.; Van Slageren, J. Improving F-Element Single Molecule Magnets. *Chem. Soc. Rev.* **2015**, *44*, 6655–6669. [CrossRef]
44. Holmberg, R.J.; Ho, L.T.A.; Ungur, L.; Korobkov, I.; Chibotaru, L.F.; Murugesu, M. Observation of Unusual Slow-Relaxation of the Magnetisation in a Gd-EDTA Chelate. *Dalton Trans.* **2015**, *44*, 20321–20325. [CrossRef] [PubMed]
45. Katoh, K.; Yasuda, N.; Damjanović, M.; Wernsdorfer, W.; Breedlove, B.K.; Yamashita, M. Manipulation of the Coordination Geometry along the C_4 Rotation Axis in a Dinuclear Tb^{3+} Triple-Decker Complex via a Supramolecular Approach. *Chem. Eur. J.* **2020**, *26*, 4805–4815. [CrossRef] [PubMed]